Realization of Anomalous Floquet Insulators in Strongly Coupled Nanophotonic Lattices

Shirin Afzal,* Tyler J. Zimmerling, Yang Ren, David Perron, and Vien Van
Department of Electrical and Computer Engineering, University of Alberta, Edmonton, Alberta T6G 2V4, Canada

(Received 24 December 2019; accepted 21 May 2020; published 24 June 2020)

We experimentally realized Floquet topological photonic insulators using a square lattice of direct-coupled octagonal resonators. Unlike previously reported topological insulator systems based on microring lattices, the nontrivial topological behaviors of our system arise directly from the periodic evolution of light around each octagon to emulate a periodically driven system. By exploiting asynchronism in the evanescent coupling between adjacent octagonal resonators, we could achieve strong and asymmetric couplings in each unit cell, which are necessary for realizing anomalous Floquet insulator behaviors. Direct imaging of scattered light from fabricated samples confirmed the existence of chiral edge states as predicted by the topological phase map of the lattice. In addition, by exploiting the frequency dispersion of the coupling coefficients, we could also observe topological phase changes of the lattice from a normal insulator to Chern and Floquet insulators. Our lattice thus provides a versatile nanophotonic system for investigating 2D Floquet topological insulators.

DOI: 10.1103/PhysRevLett.124.253601

Topological photonic insulators (TPIs) are artificial materials whose electromagnetic band structures exhibit nontrivial topological properties similar to those of electron wave functions in solid-state topological insulators [1,2]. These materials have attracted a great deal of interest recently due to their exotic properties, such as the existence of topologically protected edge modes at the sample boundaries, which could be used to realize robust optical devices and other novel applications [3–5]. Topological insulator behaviors in bosonic systems were first observed at microwave frequencies by applying an external magnetic field to a gyromagnetic photonic crystal [6]. Since the effect of the magnetic field is weak at optical frequencies, the first TPI was realized by emulating a synthetic gauge field in the form of a coupling phase gradient in a two-dimensional (2D) microring lattice [7–9]. Following these works, there have also been realizations of TPIs in zero net magnetic field by introducing a local gauge flux using next-nearest neighbor hoppings, by exploiting crystalline symmetries, or by breaking the spatial symmetry [10–15]. All of these realizations of TPIs are based on static systems with time-independent Hamiltonians whose energy bands are well characterized by the Chern number. More recently, it was shown that Floquet systems with periodically varying Hamiltonians can exhibit much richer topological properties than static systems. In particular, Floquet systems can support not only conventional Chern insulator (CI) [16,17] but also anomalous Floquet insulator (AFI) edge modes in the band gaps between energy bands with a trivial Chern number [18–23]. In addition, Floquet systems are more versatile than static systems since their topological behaviors can be tailored through suitable design of the driving Hamiltonian. AFIs have been demonstrated at acoustic and microwave frequencies using strongly coupled ring resonators [24,25], and at optical frequencies using 2D arrays of periodically coupled waveguides [26–28]. For the AFI realization based on waveguide arrays, since many periods are required to observe Floquet behaviors, the waveguides must have long lengths, typically in the range of centimeters, making them unsuitable for implementation on an integrated photonics platform.

In this Letter we report the first experimental realization of an AFI on a nanophotonics platform using a lattice of strongly coupled octagonal resonators in the silicon-on-insulator (SOI) material system. Our system exploits the periodic evolution of light around each microring to emulate a periodically varying Hamiltonian [23]. We note that our Floquet TPI lattice is fundamentally different from the microring lattice recently reported in Refs. [10,11] in that the latter realizes static Chern insulators by emulating a local gauge flux using next-nearest neighbor hoppings via off-resonant link rings between site resonators. However, since next-nearest neighbor couplings are usually weak, it is difficult to realize AFI behaviors in these lattices, which requires strong coupling to observe. In our lattice, we exploit the difference between synchronous coupling (between waveguides with the same propagation constants) and asynchronous coupling (between waveguides of different propagation constants) to achieve strong and asymmetric direct couplings in each unit cell, which enables us to observe anomalous topological effects. Direct imaging of the scattered light pattern shows clear evidence of the formation of chiral AFI edge modes in the bulk band gaps, which confirms the nontrivial topological behaviors of these lattices. In addition, by varying the coupling coefficients between the resonators, we could observe

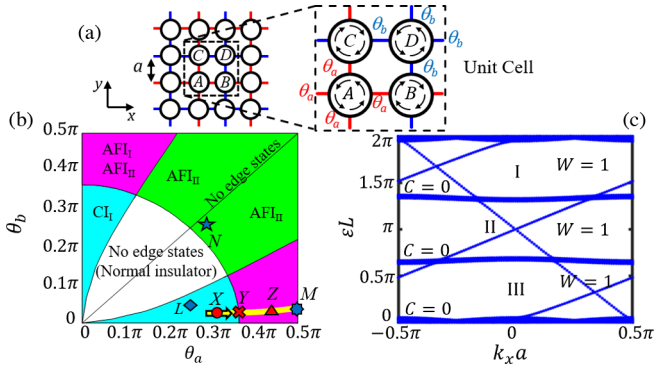

FIG. 1. (a) Schematic of a Floquet TPI microring lattice and (b) its topological phase map [23]. The lattice behaves as a normal insulator except in regions marked by CI_N or AFI_N, which denote CI or AFI behavior in band gap $N = \{I, II\}$. Markers X, Y, Z correspond to the topological phases of the fabricated lattice at three wavelengths in Fig. 5; L, M, N indicate additional fabricated lattices discussed in the Supplemental Material [29]. (c) AFI edge states in the projected quasienergy band diagram of a semi-infinite lattice with boundaries along the x direction and coupling angles $\theta_a = 0.473\pi$, $\theta_b = 0.026\pi$. The Chern number (C) of each energy band and winding number (W) of each bulk band gap are also indicated.

topological phase changes in the lattice and identify, via the formation of edge modes in the bulk band gaps, the existence of both Floquet and Chern insulators in different regions of the topological phase map. Our work thus introduces a new, versatile integrated optics platform for investigating Floquet topological behaviors in strongly coupled 2D systems.

The topological system in our study is a square lattice of direct-coupled microring resonators with identical resonance frequencies, as depicted in Fig. 1(a). Each unit cell in the lattice consists of four microring resonators, labeled A, B, C, and D, with direct adjacent neighbor couplings represented by coupling angle θ (corresponding to power coupling coefficient $\kappa^2 = \sin^2\theta$). Assuming that light in each microring propagates in only one direction, evanescent wave coupling between two neighbor resonators results in a reversal in the propagation direction, or "spin flipping." In this respect, our lattice is also different from the microring lattice in Ref. [11] (and also the acoustic and microwave lattices in Refs. [24,25]) in that the latter requires link rings for coupling between adjacent resonators to emulate a single-spin system, whereas our lattice is more compact and allows for the natural spin flipping which occurs between direct-coupled microrings. To realize nontrivial topological behaviors, we allow the coupling strengths between resonator A and its neighbors (θ_a) to be different from those between resonator D and its neighbors (θ_b). The lattice is thus characterized by two coupling angles $\theta_a \neq \theta_b$. As light circulates around each microring, it interacts periodically with its neighbors via the coupling angles θ_a and θ_b, with each period equal to one round-trip L of the microring. The lattice can thus be regarded as a periodically driven Floquet system. Its Floquet-Bloch Hamiltonian can be derived by transforming the microring lattice into an equivalent coupled waveguide array, as shown in Ref. [23] and briefly summarized in the Supplemental Material [29].

In general, the band diagram of the quasienergy ε of the microring lattice has three band gaps for every 2π change in the round-trip phase of the microrings [or one free spectral range (FSR) of the resonators]. We label these band gaps I, II, and III, with band gaps I and III being symmetric about $\varepsilon L = \pi$, as shown in the projected band diagram of a sample lattice in Fig. 1(c). By computing the Chern number associated with each quasienergy band and the winding number for each band gap [19], we can characterize the topological behavior of the lattice in each band gap as a normal insulator, CI, or AFI. Figure 1(b) shows the topological phase map of the microring lattice in band gaps I and II as functions of the coupling angles (θ_a, θ_b). Different topological behaviors can be realized by varying the coupling strengths of the lattice. In particular, AFI behavior is achieved only for strong coupling angles satisfying the approximate relation $\theta_a^2 + \theta_b^2 \gtrapprox \pi^2/8$ with $\theta_a \neq \theta_b$. Moreover, the top left and bottom right regions of the map (pink color), where the difference between θ_a and θ_b is the greatest, are the only regions in which all three band gaps are topologically nontrivial, with all exhibiting AFI behavior. These regions can thus be used to unambiguously demonstrate AFI behavior in the microring lattice. For example, for $\theta_a = 0.473\pi$ and $\theta_b = 0.026\pi$, which correspond to a lattice realized in this study, the projected band diagram of a sample with 10 unit cells in the y direction and infinite extent along x is shown in Fig. 1(c). All three bulk band gaps support edge states of the AFI type, since the winding numbers of the band gaps are nonzero even though all the energy bands have trivial Chern numbers.

In the physical implementation of the Floquet lattice, to realize a square lattice of identical microrings, the coupling gaps between the resonators must also be identical. In order to obtain unequal evanescent coupling strengths for resonators A and D in each unit cell, we used octagonal resonators with the sides having identical lengths L_s but alternating widths W_1 and W_2, as shown in Fig. 2(a). Different coupling strengths between adjacent octagons can be achieved by exploiting the difference between synchronous coupling between two waveguides with identical width and asynchronous coupling between waveguides with different widths. In the lattice, resonators A, B, and C are oriented in the same way such that coupling between A and its neighbors B and C occurs synchronously between waveguides of the same width W_1. By rotating resonator D by 45° with respect to the other three resonators, we could obtain different coupling strengths between microring D and its neighbors due to asynchronous coupling between

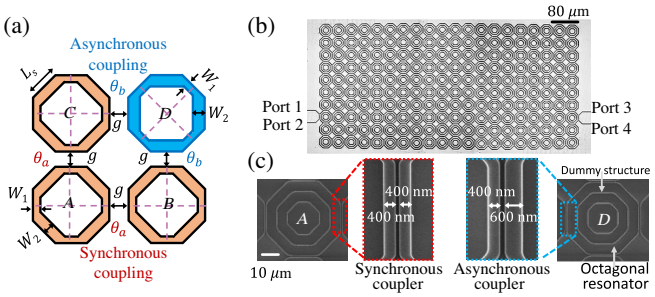

FIG. 2. (a) Schematic of a unit cell of a Floquet lattice of identical, evanescently coupled octagon resonators, with octagon D rotated by 45° with respect to the other three resonators. (b) Optical microscope image of a 5×10 fabricated lattice with input and output waveguides coupled to the left and right boundaries. (c) SEM images of octagonal resonators A and D with zoomed-in images of the synchronous and asynchronous coupling sections.

waveguides of different widths W_1 and W_2. We implemented the octagon lattice on a SOI substrate with $L_s = 16.06\ \mu$m, $W_1 = 400$ nm, $W_2 = 600$ nm, and identical coupling gap $g = 225$ nm, yielding $\theta_a = 0.473\pi$ and $\theta_b = 0.026\pi$ around 1620 nm wavelength (see Supplemental Material [29] for details). An image of the fabricated lattice consisting of 5×10 unit cells is shown in Fig. 2(b), with close-up images of the synchronous and asynchronous coupling sections in Fig. 2(c).

We characterized the transmission bands of the microring lattice by coupling TE-polarized light to the input waveguide and measuring the transmitted power in the output waveguide (see Supplemental Material [29] for details of measurement setup). Figure 3(a) shows the normalized power transmission spectrum measured over the 1620–1626 nm wavelength range. Over one FSR of the microring resonators (~5 nm), we can identify three bulk band gaps (I, II, and III) separating the passbands. The high power transmission in all three bulk band gaps indicate that edge modes are excited in these frequency ranges. We conclude that these modes must correspond to the AFI edge

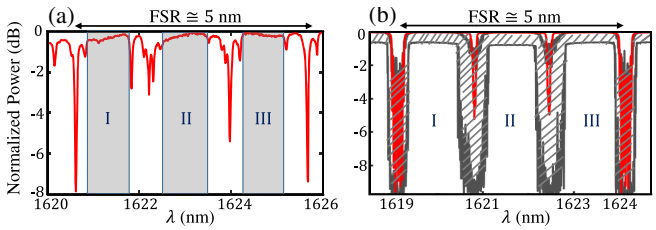

FIG. 3. (a) Measured and (b) simulated transmission spectra of the TPI microring lattice. The red line in (b) is the spectrum obtained for an ideal lattice of identical microrings with coupling angles $\theta_a = 0.473\pi$ and $\theta_b = 0.026\pi$. The hatched area indicates the range of transmission values obtained in the presence of ±5% random variations in the coupling strengths and microring round-trip phases.

states which exist in all three band gaps of the microring lattice, as predicted in the projected band diagram computed for the same lattice in Fig. 1(c). On the other hand, the transmission spectrum in the bulk passbands exhibits multiple dips, which are caused by multiple interference and localized resonances of light propagating through the bulk of the lattice. For comparison, the simulated transmission spectrum of the lattice computed using the field coupling method in Ref. [30] is shown in Fig. 3(b). The coupling angles were set at $\theta_a = 0.473\pi$ and $\theta_b = 0.026\pi$ and a propagation loss of 3 dB/cm was assumed in each resonator. The effects of ±5% uniformly distributed random variations in the coupling strengths and round-trip phases in the lattice are also shown by the hatched area in the plot. The characteristic high and flat transmission spectrum in the bulk band gaps due to edge modes are clearly visible, in good agreement with the measured spectrum. The bulk passbands also exhibit transmission dips similar to those observed in the measured spectrum. The small wavelength mismatch between the simulated and measured spectra can be attributed to a slight deviation in the effective index of the fabricated waveguides from numerical simulations, which could be caused by a systematic bias in the fabricated waveguide dimensions.

To obtain direct evidence of AFI edge modes in the bulk band gaps, we excited the lattice by injecting light at 1623 nm wavelength, which lies in band gap II, into the input waveguide and imaged the scattered light pattern using a near-infrared (NIR) camera (details in Supplemental Material [29]). Figure 4(a) shows the imaged scattered light intensity distribution over the lattice when light was injected into port 1 of the input waveguide. Clear evidence of light propagating along the bottom edge of the lattice can be seen, indicating that an AFI edge mode was formed. The simulated light intensity distribution in the microrings in Fig. 4(a) also shows good agreement with the scattered light intensity map obtained from the camera. When light was injected into port 2 of the input waveguide, a counterpropagating edge mode was excited, which propagated along the top edge of the lattice, as seen in Fig. 4(b). The two chiral modes represent two orthogonal pseudospin states of the lattice which are time-reversal (TR) counterparts of each other since they have identical quasienergy but propagate in opposite directions in each microring. However, since the driving sequence of our lattice does not satisfy the condition for TR invariance [21,31], the two chiral edge modes are not TR symmetric, as evidenced by the asymmetry in their dispersion behaviors about $k_x = 0$ and the difference in their field distributions. We also observed similar AFI edge mode patterns for excitation wavelengths in band gaps I and III. By contrast, when we tuned the laser wavelength to 1624 nm, which lies in a bulk passband, only bulk modes were excited and no edge mode was observed. This can be seen in the NIR image in Fig. 4(c), which shows that the input

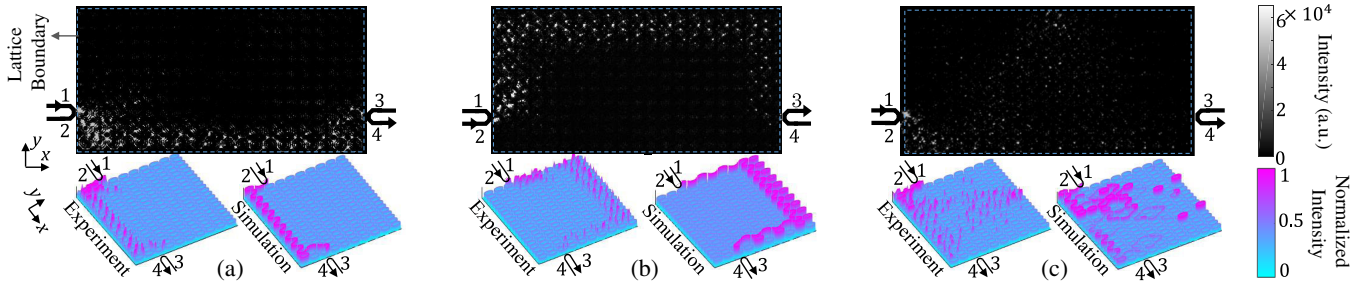

FIG. 4. (a),(b) NIR camera images showing chiral AFI edge modes along the bottom edge and top edge, respectively, of the octagon lattice when light in a bulk band gap ($\lambda = 1623$ nm) was injected into port 1 or port 2 of the input waveguide. The lower left plot in each figure shows the map of scattered light intensity constructed from raw camera data; the lower right plot is the simulated light intensity distribution in the lattice. (c) When input light was tuned to a wavelength in a transmission band ($\lambda = 1624$ nm), only bulk modes were excited and no edge mode is observed.

light spread out over the lattice instead of being localized along the edge. The simulated light intensity distribution in the lattice at the corresponding wavelength in Fig. 4(c) also confirms this behavior.

Since the topological behaviors of the microring lattice depend on the coupling angles θ_a and θ_b, we can observe topological phase changes in the lattice by exploiting the frequency dispersion of the evanescent couplers. As the wavelength is tuned from 1510 nm to 1630 nm, the simulated coupling angle increases from 0.283π to 0.495π for the synchronous coupler and from 0.014π to 0.028π for the asynchronous coupler (see Supplemental Material [29]). The corresponding topological phase of the lattice follows the yellow trajectory in Fig. 1(b), which crosses a phase boundary. Figures 5(a)–5(c) show the projected band diagrams of a semi-infinite lattice at the three sample points X, Y, and Z marked on the phase map. These points correspond to wavelengths $\lambda_X = 1532.5$ nm, $\lambda_Y = 1546.5$ nm, and $\lambda_Z = 1593.5$ nm, with coupling angles $(\theta_a;\theta_b) = (0.315\pi;0.016\pi)$, $(0.355\pi;0.018\pi)$, and $(0.430\pi;0.023\pi)$, respectively. Around wavelength λ_X, the lattice behaves as a CI in band gaps I and III and a normal insulator in band gap II. At λ_Y, band gap II closes but the lattice still retains its topological insulator behavior in band gaps I and III. Near λ_Z, the lattice supports AFI edge modes in all three band gaps.

The measured transmission spectra of the lattice around these three wavelengths are shown in Figs. 5(d)–5(f), from which close correspondence to the projected band diagrams can be observed. In particular, high transmission is observed in wavelength ranges corresponding to topologically nontrivial bulk band gaps where CI or AFI edge modes are expected. Within one FSR of the microring resonators, transmission spectra X and Y show only two bulk band gaps (I and III) with edge modes while spectrum Z has three distinct bulk band gaps with edge modes, as predicted by the projected band diagrams. For spectrum X, the transmission in the center bulk band gap (band gap II) is low since the lattice behaves as a normal insulator and thus no edge mode exists. This behavior is confirmed by the scattered light distribution imaged at $\lambda = 1532.80$ nm in Fig. 5(g), showing input light being reflected from the lattice. However, at $\lambda = 1534.67$ nm, which lies in band gap III of spectrum X, the lattice behaves as a CI, as evidenced by the edge mode imaged at $\lambda = 1534.67$ nm in Fig. 5(h). As the wavelength is tuned from λ_X to λ_Y, the center band gap closes [Fig. 5(e)], although transmission in the output waveguide remains low since light can propagate throughout the lattice and is partially reflected back into the input waveguide. This can be seen in the NIR image at $\lambda = 1546.50$ nm in Fig. 5(i). As the wavelength is further

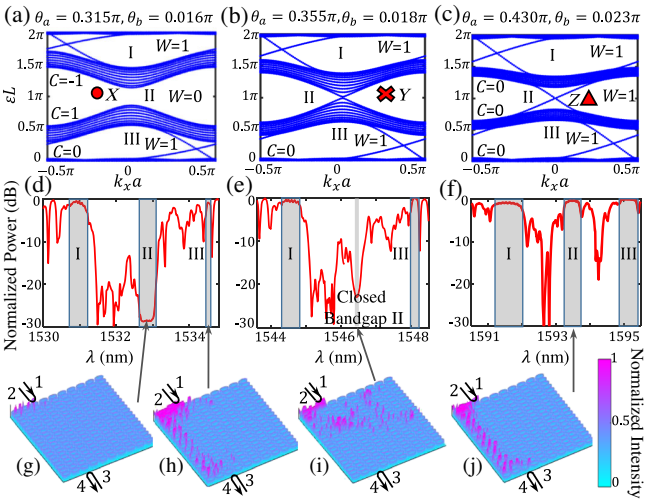

FIG. 5. Topological phase changes in the octagon lattice due to frequency dispersion in the coupling angles: (a)–(c) Projected band diagrams of a semi-infinite lattice with boundaries along x around (a) $\lambda_X = 1532.5$ nm, (b) $\lambda_Y = 1546.5$ nm, (c) $\lambda_Z = 1593.5$ nm. (d)–(f) Measured transmission spectra of the lattice over one FSR centered around λ_X, λ_Y, and λ_Z. (g)–(j) Scattered light intensity distributions obtained from NIR camera showing different topological behaviors at various input wavelengths: (g) normal insulator located in topologically trivial bulk band gap II, (h) CI edge mode in bulk band gap III, (i) bulk modes in closed band gap II, (j) AFI edge mode in reopened bulk band gap II.

increased to λ_Z [Fig. 5(f)], the center band gap opens again but with an important difference in that the transmission in the band gap is now high due to the formation of an AFI edge mode, as verified by the NIR image at $\lambda = 1593.50$ nm in Fig. 5(j).

We also fabricated octagon lattices with different coupling gap, coupling length, and waveguide widths to verify the topological behaviors of the lattice in the different regions of the phase map in Fig. 1(b). These samples are marked L, M, and N on the map. NIR images also showed edge modes formed in topologically nontrivial band gaps of these lattices as predicted by the phase map. These results, which are included in the Supplemental Material [29], also provide additional evidence that our Floquet microring lattice behaves as predicted.

In conclusion, we experimentally demonstrated a Floquet TPI based on a 2D lattice of strongly coupled octagonal resonators. The system emulates a periodically varying Hamiltonian through the periodic evolution of light around each octagon. By exploiting asynchronism in the evanescent coupling between waveguides of different widths, we could realize strong and asymmetric direct couplings between adjacent resonators, which allows us to observe chiral AFI edge modes. Our lattice also exhibits rich topological behaviors, including a normal insulator, CI, and AFI, by tuning the coupling angles. Our work thus introduces a versatile nanophotonic platform for investigating Floquet TPIs and exploring their applications.

This work was supported by the Natural Sciences and Engineering Research Council of Canada.

*safzal1@ualberta.ca

[1] L. Lu, J. D. Joannopoulos, and M. Soljačić, Nat. Phys. **12**, 626 (2016).

[2] T. Ozawa, H. M. Price, A. Amo, N. Goldman, M. Hafezi, L. Lu, M. C. Rechtsman, D. Schuster, J. Simon, O. Zilberberg, and I. Carusotto, Rev. Mod. Phys. **91**, 015006 (2019).

[3] B. Bahari, A. Ndao, F. Vallini, A. El Amili, Y. Fainman, and B. Kanté, Science **358**, 636 (2017).

[4] M. A. Bandres, S. Wittek, G. Harari, M. Parto, J. Ren, M. Segev, D. N. Christodoulides, and M. Khajavikhan, Science **359**, eaar4005 (2018).

[5] Y. Wang, X. L. Pang, Y. H. Lu, J. Gao, Y. J. Chang, L. F. Qiao, Z. Q. Jiao, H. Tang, and X. M. Jin, Optica **6**, 955 (2019).

[6] Z. Wang, Y. D. Chong, J. D. Joannopoulos, and M. Soljačić, Nature (London) **461**, 772 (2009).

[7] M. Hafezi, E. A. Demler, M. D. Lukin, and J. M. Taylor, Nat. Phys. **7**, 907 (2011).

[8] M. Hafezi, S. Mittal, J. Fan, A. Migdall, and J. M. Taylor, Nat. Photonics **7**, 1001 (2013).

[9] S. Mittal, J. Fan, S. Faez, A. Migdall, J. M. Taylor, and M. Hafezi, Phys. Rev. Lett. **113**, 087403 (2014).

[10] D. Leykam, S. Mittal, M. Hafezi, and Y. D. Chong, Phys. Rev. Lett. **121**, 023901 (2018).

[11] S. Mittal, V. V. Orre, D. Leykam, Y. D. Chong, and M. Hafezi, Phys. Rev. Lett. **123**, 043201 (2019).

[12] S. Barik, A. Karasahin, C. Flower, T. Cai, H. Miyake, W. DeGottardi, M. Hafezi, and E. Waks, Science **359**, 666 (2018).

[13] J. Noh, S. Huang, K. P. Chen, and M. C. Rechtsman, Phys. Rev. Lett. **120**, 063902 (2018).

[14] M. I. Shalaev, W. Walasik, A. Tsukernik, Y. Xu, and N. M. Litchinitser, Nat. Nanotechnol. **14**, 31 (2019).

[15] X. T. He, E. T. Liang, J. J. Yuan, H. Y. Qiu, X. D. Chen, F. L. Zhao, and J. W. Dong, Nat. Commun. **10**, 872 (2019).

[16] K. Fang, Z. Yu, and S. Fan, Nat. Photonics **6**, 782 (2012).

[17] M. C. Rechtsman, J. M. Zeuner, Y. Plotnik, Y. Lumer, D. Podolsky, F. Dreisow, S. Nolte, M. Segev, and A. Szameit, Nature (London) **496**, 196 (2013).

[18] T. Kitagawa, E. Berg, M. Rudner, and E. Demler, Phys. Rev. B **82**, 235114 (2010).

[19] M. S. Rudner, N. H. Lindner, E. Berg, and M. Levin, Phys. Rev. X **3**, 031005 (2013).

[20] M. Pasek and Y. D. Chong, Phys. Rev. B **89**, 075113 (2014).

[21] F. Nathan and M. S. Rudner, New J. Phys. **17**, 125014 (2015).

[22] D. Leykam, M. C. Rechtsman, and Y. D. Chong, Phys. Rev. Lett. **117**, 013902 (2016).

[23] S. Afzal and V. Van, Opt. Express **26**, 14567 (2018).

[24] Y. G. Peng, C. Z. Qin, D. G. Zhao, Y. X. Shen, X. Y. Xu, M. Bao, H. Jia, and X. F. Zhu, Nat. Commun. **7**, 13368 (2016).

[25] F. Gao, Z. Gao, X. Shi, Z. Yang, X. Lin, H. Xu, J. D. Joannopoulos, M. Soljačić, H. Chen, L. Lu, and Y. D. Chong, Nat. Commun. **7**, 11619 (2016).

[26] L. J. Maczewsky, J. M. Zeuner, S. Nolte, and A. Szameit, Nat. Commun. **8**, 13756 (2017).

[27] S. Mukherjee, A. Spracklen, M. Valiente, E. Andersson, P. Öhberg, N. Goldman, and R. R. Thomson, Nat. Commun. **8**, 13918 (2017).

[28] S. Mukherjee, H. K. Chandrasekharan, P. Öhberg, N. Goldman, and R. R. Thomson, Nat. Commun. **9**, 4209 (2018).

[29] See Supplemental Material at http://link.aps.org/supplemental/10.1103/PhysRevLett.124.253601 for details of the derivation of the periodic Hamiltonian of a Floquet microring lattice, implementation of Floquet octagon lattices on a silicon-on-insulator platform, experimental setup, and additional evidence of topological edge modes in octagon lattices with other coupling parameters.

[30] A. Tsay and V. Van, IEEE J. Quantum Electron. **47**, 997 (2011).

[31] B. Höckendorf, A. Alvermann, and H. Fehske, Phys. Rev. B **99**, 245102 (2019).